A Combined NMR and Molecular Dynamics Study of Methane Adsorptive Behavior in M_2(dobdc)

Velencia J. Witherspoon,[†,‡] Rocío Mercado,[†,¶] Efrem Braun,[‡] Amber Mace,[§] Jonathan Bachman,[‡] Jeffrey R. Long,[¶,‡] Bernhard Blümich,[‖] Berend Smit,[§,‡] and Jeffrey A. Reimer[*,‡,⊥]

† *Joint first authors.*

‡ *Department of Chemical and Biomolecular Engineering, University of California, Berkeley, Berkeley, CA 94720, USA*

¶*Department of Chemistry, University of California, Berkeley, Berkeley, CA 94720, USA*

§*Institut des Sciences et Ingénierie Chimiques, Valais, École Polytechnique Fédérale de Lausanne (EPFL), Rue de l'Industrie 17, CH-1951 Sion, Switzerland*

‖ *Institut für Technische und Makromolekulare Chemie (ITMC), RWTH Aachen University, 52062 Aachen, Germany*

⊥*Materials Science Division, Lawrence Berkeley National Laboratory, Berkeley, CA 94720, USA*

E-mail: reimer@berkeley.edu

Abstract

We examine the diffusion of methane in the metal–organic frameworks M_2(dobdc) (M = Mg, Ni, Zn; $dobdc^{4-}$ = 2,5-dioxido-1,4-benzenedicarboxylate) as a function of methane loading through a combination of nuclear magnetic resonance (NMR) and

molecular dynamics simulations. At low gas densities, our results suggest that favorable CH_4–CH_4 interactions lower the free energy barrier for methane hopping between coordinatively unsaturated metal sites and thus enhance the translational motion of methane down the *c*-axis. At higher gas loadings, CH_4–CH_4 interactions become more significant, and as CH_4–CH_4 collisions become more frequent, the gas self-diffusion begins to decrease. Finally, we observe that the self-diffusion coefficient of methane is inversely related to the binding energy at the coordinatively unsaturated metal sites, such that diffusion is most rapid in the Zn_2(dobdc) framework and slowest in the Ni_2(dobdc) framework.

Introduction

Metal–organic frameworks are porous, three-dimensional solids consisting of metal nodes connected by organic linkers, and their immense synthetic and topological diversity has rendered them exceptional candidates for the selective capture and separation of small molecules, including carbon dioxide, methane, and xenon.[1–6] For a number of such materials, known as isoreticular frameworks, it is possible to vary the metal ion and/or linker while maintaining the parent topology, therefore enabling systematic variation of material composition and properties such as pore size.

One such family of isoreticular structures is the M_2(dobdc) series of frameworks (also known as M-MOF-74; M = Mg, Mn, Fe, Co, Ni, Cu, or Zn; $dobdc^{4-}$ = 2,5-dioxodo-1-4-benzenedicarboxylate), which has been widely studied for applications in gas storage and separation due to the presence of coordinatively unsaturated or "open" metal sites that are able to strongly bind and polarize various gases.[7–13] Further tailoring of this class of materials to exhibit selective CH_4 interactions is of interest for establishing highly efficient adsorptive separation processes for applications in natural gas enrichment and the separation of CH_4 from power plant flue gas mixtures,[10,14,15] as well as toward the development of alternatives for natural gas storage in transportation vehicles.[10,16] Motivated by these

applications, previous research has investigated the potential of M_2(dobdc) frameworks for the storage and separation of methane and demonstrated that the choice of transition metal can significantly influence the material adsorptive capacity.[10,16] In particular, the Ni_2(dobdc) analogue displays the highest volumetric methane uptake of 230 v STP/v at 35 bar, followed by Mg_2(dobdc) and Zn_2(dobdc) (200 v STP/v and 188 v STP/v at 35 bar, respectively).[10,16] Neutron scattering characterization of CH_4 adsorption in M_2(dobdc) has shed light on this result, revealing that the primary adsorption site is located directly above the coordinatively unsaturated metal centers, while a secondary site exists along the *c*-axis between the primary sites.[13] A tertiary binding site has also been located in the center of the pores for methane and certain other adsorbates.[17] At low pressures, the various M_2(dobdc) analogues exhibit differences in CH_4 uptake that primarily arise due to differences in gas binding energies at the open metal sites.

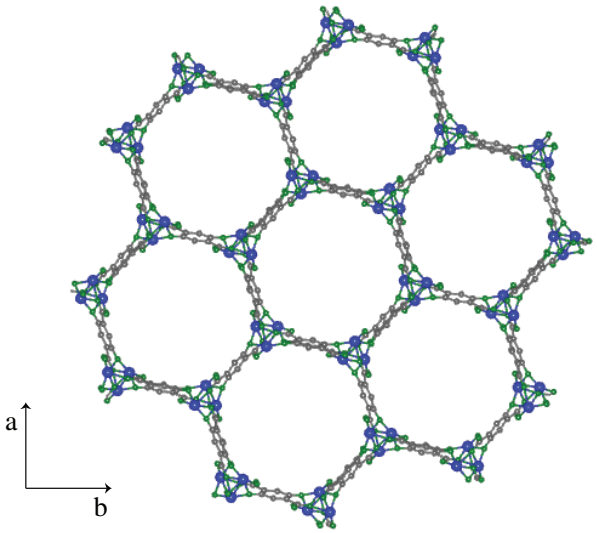

Figure 1: Illustration of the M_2(dobdc) structure with one-dimensional pores extending along the *c*-axis. Gray, green, and blue spheres represent C, O, and M atoms, respectively. Hydrogen atoms are omitted for clarity.

Computational investigations have also found that the relative binding energy of CH_4 at the open metal sites in M_2(dobdc) (M = Mg, Ni, and Zn) is highest in the Ni analogue, followed by the Mg analogue and finally the Zn analogue, in agreement with experimental

results.[16,18] These studies also reported differences in the binding energies associated with the secondary adsorption sites. Further, analysis of spatial probability distributions produced from grand canonical Monte Carlo (GCMC) simulation data have predicted that CH_4 molecules spend a larger fraction of their time near the open metal sites in frameworks with stronger heats of adsorption — in contrast to frameworks that lack such strong adsorption sites where the adsorbate instead spends a greater amount of time in the center of the pores, away from the framework walls.[16]

While many studies have indirectly evaluated the effect of energetics on the suitability of a system for gas separations (e.g., by fitting transient breakthrough data), few studies have systematically studied the effect of host-guest energetics on mass transport in metal–organic frameworks.[19] The transport of CH_4 in Ni_2(dobdc) was investigated previously via permeation experiments for mixed-membrane applications, where it was found that these macroscopic methods yielded averaged mass transfer coefficients with contributions from both the intercrystalline and intracrystalline regimes.[20] However, it was not possible to separate these contributions using that experimental method. Understanding the transport contributions of small molecules in metal–organic frameworks has in general proven challenging, with few experimental techniques available to assess mass transfer coefficients associated with the intracrystalline regime.[21] In this regime, systematic variations in pore features such as size and metal binding site can greatly influence mass transfer.

Nuclear magnetic resonance (NMR)[22] is a robust technique that has proven valuable in understanding the motion of adsorbed gases, for instance by providing access to individual self-diffusion coefficients (D_s) and relaxation rate constants for a given adsorbate.[23–27] Furthermore, molecular dynamics (MD) simulations[27,28] performed as a function of adsorbate loading in a number of metal–organic frameworks have indicated that the observed magnitude of intracrystalline D_s depends strongly on the interaction strength of the adsorbate with the framework.[29] Here, we seek to use these methods in tandem to develop an enhanced understanding of methane adsorption dynamics in M_2(dobdc), with MD simula-

tions complementing the NMR data at conditions that are not experimentally accessible. These complementary methods reveal that at low methane loadings, increasing the density of methane molecules in the pores leads to a decrease in the free energy barrier between metal sites and an increase in molecule diffusivity, whereas at high methane loadings, an increase in gas density disrupts the paths of other methane molecules and decreases their diffusivity. Similarly, the open metal sites decrease the diffusivity of methane in the pores by interrupting CH_4 trajectories in proportion to the metal–CH_4 binding strength.

Methods

NMR Sample Preparation The M_2(dobdc) analogues were prepared via the previously reported routes[30] yielding crystal sizes between 10 and 20 μm. For each analogue, the as-synthesized material was activated and transfered to an argon glovebox before being loaded into a valved NMR tube. The samples were then activated again for 12 hours at 180 °C and 0.01 mbar. Following activation,[1] the samples were cooled to 40 °C and held at the desired equilibrium pressure for thirty minutes to an hour before closing the valve on the NMR tube. The sample was then allowed to cool to room temperature and transferred to the NMR probe where it was re-heated to 40 °C for thirty minutes before data collection.

NMR Measurements A 13 Interval Bi-Polar Pulse Field Gradient Stimulated Echo experiment with z-spoiler was performed with a Bruker Avance III 700 MHz spectrometer using a Diff30 insert in the Mic5 Bruker imaging probe, as described previously.[31] Diffusion times ranged from 1 – 2.5 ms while the gradient strength ranged from 0 – 17 T/m in 48 steps. The observed attenuation was processed using a one-dimensional inverse Laplace transformation as implemented in the Kea Prospa software. The reported experimental values are the average of the logarithm mean of the resulting Inverse Laplace transforms. Each loading condition was sampled 3 – 5 times, with error bars representing the standard deviation of these measurements. The longitudinal, or spin-lattice, relaxation rate constant

(R_1) was obtained using an Inversion Recovery Pulse Sequence (180-90-Acquire) and the transverse relaxation rate constant (R_2) was measured by implementing the Carr-Purcell-Meiboom-Gill pulse sequence with spectroscopic aquisitions.[32] For all sample loadings, R_1 was smaller than R_2 and the stimulated echo diffusion rate was significantly greater than both R_1 and R_2. The diffusion time was limited to 2.5 ms due to evidence of potential diffusive diffraction[33] at longer times.

MD Simulations The self-diffusion coefficients were computed for CH_4 diffusion in M_2(dobdc) (M = Mg, Ni, Zn) from MD simulations performed using LAMMPS.[34,35] The systems were simulated in the canonical ensemble at loadings corresponding to the equilibrium uptake values as determined from GCMC simulations at pressures ranging from 0.1 – 100 bar and 313 K (Table S5; Figure S3). After equilibration for 1 ns, each system was simulated for 10 ns with a timestep of 1 fs using a Nosé-Hoover thermostat. For framework–CH_4 interactions, a previously parameterized density functional theory (DFT) derived force field[16] was used. Methane–methane interactions were taken from TraPPE.[36] Non-bonding interactions were cut-off and shifted at 12.5 Å, and all unit cells were sufficiently replicated so as to avoid interaction between periodic replica.

The values of D_s for adsorbed CH_4 were computed from these equilibrium simulations using the Einstein equation, which relates the self-diffusivity of a molecule to its mean-squared displacement (MSD). In particular, D_s values were calculated from methane MSDs in each framework in the diffusive regime (2 – 100 ps) as generated using the order-n algorithm previously described.[37,38]

At the lowest CH_4 loadings considered in this work ($\sim$ 0.027 CH_4/M^{2+}), simulations would consist of boxes containing only one or two CH_4 molecules if carried out in the same manner as those simulations at the higher loadings. Such a simulation is problematic because both the temperature and distribution of molecules within the pores — six pores per simulation supercell — are not well-defined for only a single (few) particle(s). To address these concerns and to establish that the D_s values at these low pressures are better defined,

simulations at the same low CH_4 densities corresponding to the lowest pressure simulations in each framework (0.027 CH_4/M^{2+}) were carried out, but with increasing c-axis lengths, l, of the simulation supercell (where $l \in \{4, 8, 12, 16, 20, 24, 28, 32\}$), and with increasing numbers of CH_4 atoms, N, in the pores (N or $2N$ per pore, uniformly distributed, where $N \in \{1, 2, 3, 4, 5, 6, 7, 8\}$). The D_s was then extrapolated from the converged value corresponding to an infinitely-long simulation box.

For the lowest density simulations in each M_2(dobdc) framework, which were more expensive due to their size, the error bars for the D_s values were estimated by dividing each 10 ns trajectory into ten 1 ns trajectories and calculating the standard deviation of the ten D_s values computed for each 1 ns trajectory. For all other higher density trajectories, the error bars for the D_s magnitudes were estimated by running three different simulations at the same set of conditions and calculating the standard deviation of the three D_s values computed for each 10 ns trajectory.

Probability Densities The probability densities of adsorbed CH_4 in all three M_2(dobdc) frameworks were computed by binning CH_4 positions from the 10 ns trajectories onto a $0.2 \times 0.2 \times 0.2$ Å^3 grid using PEGrid[39] and plotted in VisIt.[40]

Methane Hopping Rates In order to estimate the hopping rate of CH_4 between the primary and secondary binding sites in each M_2(dobdc) framework, the average exchange rate was calculated by counting the number of times a CH_4 molecule transitioned from a primary binding site (2.8 – 3.0 Å from the metal) to a secondary binding site (3.5 – 3.7 Å from the metal), or vice versa, per ns of time. The methane distances from each binding site were determined from the spatial distribution of CH_4 around the metals; peaks in the CH_4 density corresponding to the two densest binding sites occurred near 2.9 Å and 3.6 Å for all three frameworks (see Figures S12 – S17 in SI section *Methane Binding Site Analysis* for details). A width of 0.2 Å around the peak density of each binding site was chosen such that the CH_4 binding site would be unambiguous. For example, if a CH_4 molecule crossed into the intermediate region (between 3.0 – 3.5 Å), and then back to the same site, this was

not counted as an exchange event.

Free Energy Calculations To estimate the free energy barrier for hopping between adjacent metal sites, both down the c-axis (supercell axis in line with the z-axis for a single unit cell) and along a given ab-plane (orthogonal to the c-axis), MD simulations were carried out at loadings of 2 – 14 CH_4 molecules per pore in each M_2(dobdc) framework. The MD simulations were run for 10 ns, saving the positions of the adsorbates every MD cycle.

The positions of the adsorbates in a single pore were mapped to one unit cell along the c-axis and binned to a $0.4 \times 0.4 \times 0.4$ Å^3 grid. An "in-house" algorithm was then used to partition the free energy grid into separate potential energy wells and to identify the transition states which separate these. This provides the necessary information to compute the free energy barriers and estimate D_s analytically by applying transition state theory based Bennett-Chandler method[41,42] for the transitions along the c-axis and within the ring. Here, D_s along the c-axis indicates a "true" diffusion of the CH_4 traveling through the material, while the D_s for the "ring-like" diffusion does not.

To test the hypothesis that the presence of a CH_4 lowers the energy barriers for CH_4 diffusion in surrounding diffusion channels parallel with the c-axis, we compare the potential energy surfaces (PES) of CH_4 within the field of the framework alone and with that with a CH_4 particle placed at a primary adsortion site. The PES is derived from Monte Carlo simulations where 100 million single particle insertions are carried out in the canonical ensemble to sample the energetic space. The coordinates are saved at every step and treated the same way as the MD coordinates to create a 3D grid quantifying the PES. This procedure is first carried out on an the empty framework and from the resulting PES grid, the coordinates corresponding to the minimum of a potential energy well of a primary adsorption site are identified where a CH_4 particle is positioned within the framework and the PES is computed for this derived framework. The energy barriers for the c-axis transitions are computed from the two PES grids using the partitioning algorithm to compare how these are altered in the field of another adsorbate.

Results and Discussion

The relaxation of free and adsorbed molecules within a metal–organic framework is mediated by various spin-lattice relaxation mechanisms, which may be dominated by intramolecular, intermolecular, and spin-rotation interactions. In NMR, intramolecular interactions predominately exist in the form of dipole-dipole interactions between ^{1}H–^{1}H and ^{1}H–^{13}C pairs in a single molecule. These interactions may be neglected for most pure gases near or above room temperature. For example, in 1971 researchers showed through deuterium dilution experiments (using CH_3D, CH_2D_2, and CHD_3) that contributions from intramolecular proton interactions became neglible near room temperature for the spin-lattice relaxation of CH_4.[43,44] Contributions from chemical shift anisotropy are important for the observation of nuclei that can exhibit large chemical shifts, but this scenario does not apply to CH_4 due to the very narrow proton chemical shift range. Intermolecular interactions may be due to ^{1}H–^{1}H or ^{1}H–metal and ^{1}H–^{13}C pairwise interactions between different CH_4 molecules or between CH_4 and framework atoms, respectively. Finally, spin-rotation relaxation is often considered to be dominant for gaseous species and derives from the coupling between molecular rotational angular momentum and the nuclear spin.[45,46]

Relaxation that is dominated by spin-rotation gives rise to relaxation rates that are sensitive to gas density. In the low-density regime for pure gases, it has been found that the relaxation rate correlates with the number of binary collisions.[43] As the collision frequency increases, molecular impacts perturb the angular momentum, effectively shortening the correlation time and leading to a maximum in the spin-lattice relaxation rate (R_1); this maximum occurs when the nuclear Larmor frequency and the collision frequency are equal. Beyond this point, the observed R_1 may enter the reciprocal regime, where its value decreases linearly with the gas density due to the increase in dipole-dipole coupling between neighboring molecules.

For pure CH_4 at 193 K, it has been shown that a transition from a low to a high density regime takes place at 193 bar; however, this transition was not observed at room temper-

ature.[47] Previous work has also demonstrated that R_1 decreases linearly with increasing adsorbed-phase density of CH_4 in ZIF-8, a MOF with no coordinatively unsaturated metal sites.[26] It was proposed that the spin-rotation mechanism is influenced by interactions with the framework, and a surface relaxivity term, ρ_s, was introduced to describe the slope of the observed spin-lattice relaxation rates with increasing adsorbed phase density in the frameworks. Thus, the relative difference in ρ_s for similar MOF archetypes is proportional to the strength of interaction between the frameworks and the adsorbed gases.

On the other hand, in porous media, contributions from intermolecular interactions are more significant at higher loadings due to the increased proximity of CH_4–based ^1H nuclei to other nuclei. As the primary binding sites in M_2(dobdc) (located at the coordinatively unsaturated metals) become occupied, CH_4 molecules are forced to occupy weaker binding sites in the pores. Exchange between primary and secondary adsorption sites, as well as exchange between bound and free CH_4, consequentially decreases the spin-rotational correlation times. This behavior is not expected to occur for non-adsorbed CH_4 gas until pressures of 193 bar are reached, but manifest in confined CH_4 at lower equilibrium pressures due to interactions with the framework.[44]

In contrast to a previous study that found the longitudinal CH_4 relaxation rate decreases with increasing density in certain porous media,[26] we found that the R_1 for CH_4 gas in M_2(dobdc) initially increases with increasing density at low pressures (Figure 2, top) and then decreases. Whereas in pure gas a collision is the only interaction strong enough to interrupt the rotational trajectory of a molecule, for confined CH_4 at low density the angular momentum is more likely to be interrupted by adsorption at the metal site. This behavior may be attributed to the initial binding of the gas molecules directly above the coordinatively unsaturated metal sites.[16,17] For M_2(dobdc) (M = Mg, Ni, Zn), at pressures below 10 bar in all three metal frameworks considered, the primary sites remain undersaturated, and the probability of finding a molecule at a coordinatively unsaturated metal site is still higher than the probability of finding it elsewhere in the pore. According to GCMC

simulations, the coordinatively unsaturated metal sites remain unoccupied until approximately 10 – 20 bar, depending on the framework (Tables S2 – S4). In this low pressure regime, rotational diffusion is mainly influenced by the CH_4 hopping frequency between the coordinatively unsaturated metal sites, or the free energy barrier for translational motion. This phenomenon has been observed for adsorbed liquid species and is often referred to as *reorientations mediated by translational displacements*.[48]

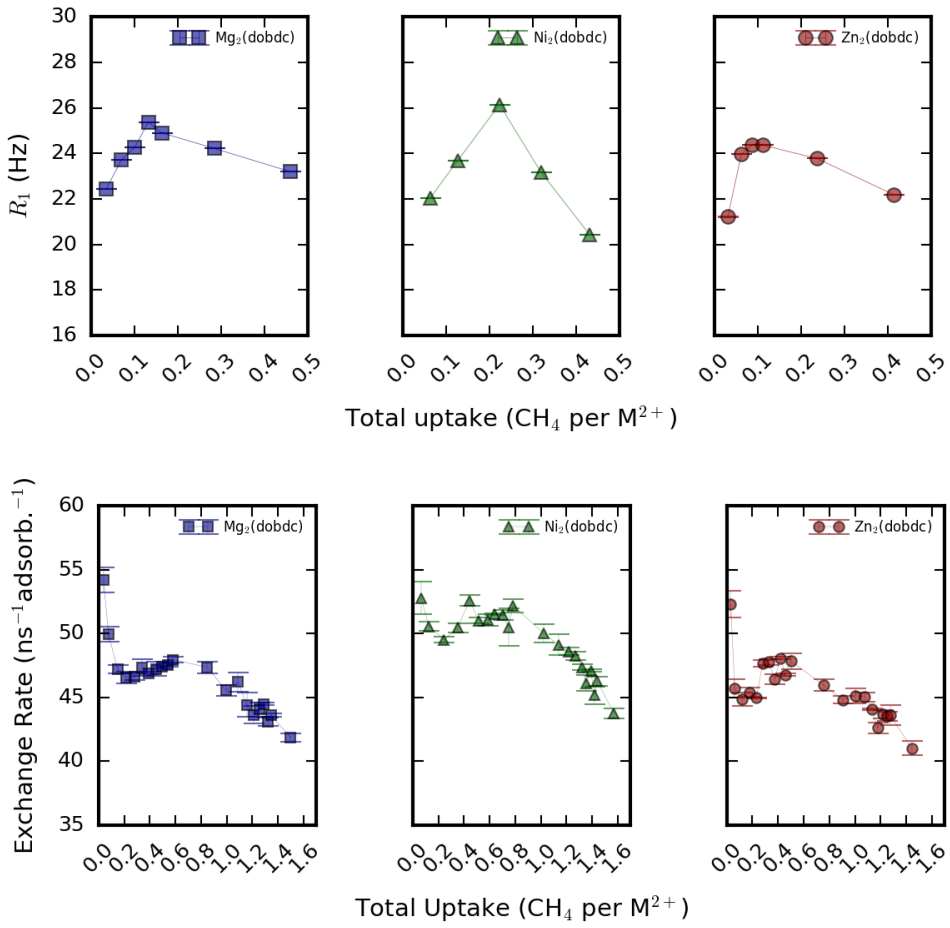

Figure 2: (top) Values of the longitudinal relaxation time, R_1, for CH_4 adsorbed in M_2(dobdc) (M = Mg, Ni, and Zn) as a function of methane loading per coordinatively unsaturated metal site. Interpolated lines are shown as guides for the eye. (bottom) Exchange rates between the primary and secondary binding sites calculated from MD simulations in each framework. All experiments and simulations were carried out at 313 K. Note the different axes scales for the experimental and simulated data.

The D_s coefficients calculated from simulation in M_2(dobdc) are shown in Figure 3.

We found that the diffusion coefficient increases in magnitude at low pressures, peaks at an uptake of 0.17 CH_4/M^{2+}, and then decreases again. The initial increase in D_s at low methane loadings may arise due to a decrease in the free energy barrier for hopping between open metal sites, as calculated using MD simulations (Figure 4). While it is well known that the heat of adsorption of methane increases in the presence of additional methane molecules due to favorable CH_4–CH_4 interactions, it is not straightforward that this should be accompanied by a decrease in the free energy barrier between the primary binding sites, as has been demonstrated here for M_2(dobdc).

With increasing CH_4 loading in each framework, R_1 passes through a maximum that can be inversely correlated with the binding energy of the gas at a given metal site — i.e., for the framework with the largest metal–site binding energy, Ni_2(dobdc), a maximum occurs at a loading of ~ 0.2 CH_4 per metal site, followed by maxima at loadings of ~ 0.15 and ~ 0.09 CH_4 per metal site in the Mg and Zn analogues, respectively (Figure 2). This magnitude of R_1 is qualitatively representative of the frequency of an adsorption event, analogous to the frequency of collisions for free gases, and this trend indicates that the maximum frequency increases as the binding strength also increases. However, at loadings below the maxima in R_1 in the Ni framework, it is evident that the weaker metal–CH_4 interactions in Zn- and Mg_2(dobdc) allow for more CH_4–CH_4 collisions or interactions inside the framework pores. From NMR relaxation experiments, the CH_4 collision rates at the maximum value of R_1 were determined to be approximately 26.1, 25.4, and 24.4 Hz in Ni_2(dobdc), Mg_2(dobdc), and Zn_2(dobdc) at 40 °C. This trend for R_1 can be correlated with relative methane adsorption enthalpies in each framework — for example, the adsorption enthalpies at a loading of 0.2 CH_4/M^{2+} are 21.0, 18.6, and 16 kJ/mol for Ni_2(dobdc), Mg_2(dobdc), and Zn_2(dobdc), respectively.[10,49]

The exchange rate between primary and secondary binding sites was also calculated as a function of CH_4 metal-site loading using MD simulations (Figure 2, bottom). Here, the primary binding site was defined as being at a distance of 2.8 – 3.0 Å from the metal

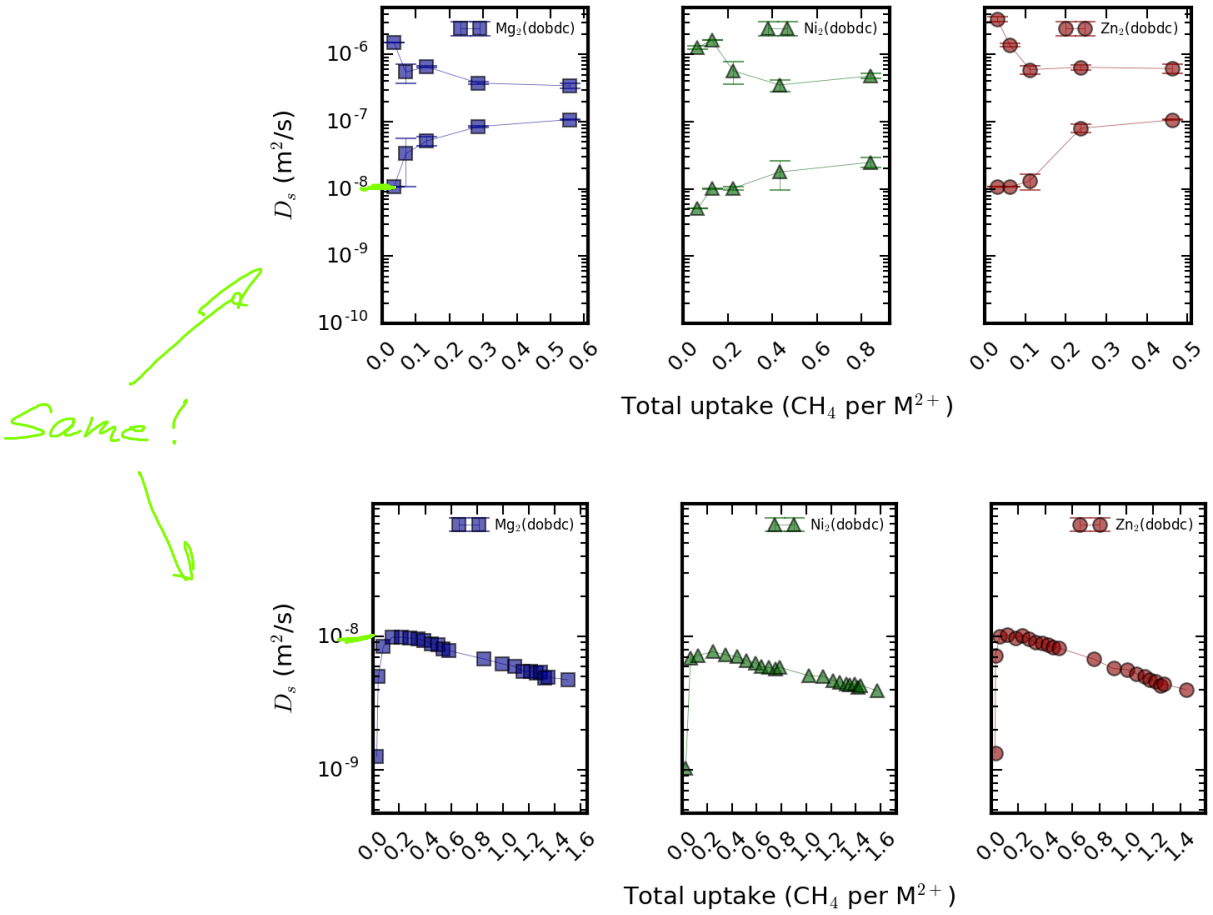

Figure 3: (top) Experimental values of the methane self-diffusion coefficient, D_{s}, in M_2(dobdc) (M = Mg, Ni, and Zn) as measured by NMR for 2 ms diffusion times. The larger D_{s} values are attributed to intercrystalline diffusion, whereas the smaller values are attributed to intracrystalline diffusion. (bottom) Simulated D_{s} values obtained from 1 ns MD trajectories. Note the different axes scales.

and the secondary binding site was defined as 3.5 – 3.7 Å away from the metal. At the lowest loadings — between 0.01 and 0.16 CH_4/M^{2+} — the simulated exchange rates initially decrease significantly for all three frameworks, a trend which is not experimentally observed. For low to moderate loadings, the trend in the calculated exchange rates is in closer agreement with experimental measurements — i.e., exchange between the two sites is in general fastest in the Ni_2(dobdc) framework and slowest in the Zn_2(dobdc) framework under nearly all conditions. Also in agreement with experiments, we found that the exchange rate between the primary and secondary binding sites in simulations is greatest in Ni_2(dobdc) and smallest in Zn_2(dobdc). This result is interesting given that the CH_4 heat of adsorption is larger in Ni_2(dobdc) than in the other two frameworks considered. However, the greater exchange in the Ni framework serves to further support the overall lower D_s values at all CH_4 loadings in this material relative to the Zn framework, because a greater frequency of exchange events is analogous to a greater number of collisions. For loadings greater than 0.16 CH_4/M^{2+}, the simulated exchange rates steadily increase in all three frameworks before decreasing again beyond loadings of 0.8 CH_4/M^{2+}.

Analysis of the pulsed field gradient NMR data revealed binary self-diffusion coefficients associated with the existence of two populations of CH_4 — one that experiences fast diffusion on the order of 10^{-7} m^2/s, and one that undergoes much slower diffusion on the order of 10^{-9} m^2/s. We propose that the fast self-diffusion measured via NMR can be attributed to the faster exchange between adsorbed and intercrystalline CH_4, whereas the slow diffusion can be attributed to movement of CH_4 within a single crystallite. We note that all analogues of M_2(dobdc) possess small crystal sizes — approximately 10 μm in length and a few microns in width for the as-synthesized powders — such that the diffusive path of a molecule can still be hundreds of microns in length in a 2.5 ms experimental diffusion time.

At all loadings examined in the simulations, the magnitudes of the intracrystalline D_s are greatest in Zn_2(dobdc), followed by Mg_2(dobdc) and Ni_2(dobdc). On the other hand, experimental measurements at low pressures show that the magnitudes of the intracrystalline

D_s were greatest in Mg_2(dobdc), followed by Zn_2(dobdc) and Ni_2(dobdc). Nonetheless, the overall trend is not surprising, as it suggests that a weaker interaction between CH_4 and metal sites (such as in the Zn and Mg materials) allows for faster translational motion. Furthermore, translational motion is hindered when there is a stronger interaction between CH_4 and the open metal sites, such as in Ni_2(dobdc). These results are in agreement with the relaxation behavior, which indicates that rotational diffusion is mediated by frequent translational displacements.

In order to investigate whether D_s would increase after saturation of all the primary binding sites, we also carried out MD simulations where the number of CH_4 molecules per unit cell exceeded that of the open metal centers. As mentioned above, from these simulations we found that the intracrystalline D_s value increases for loadings between 0.01 to 0.2 CH_4/M^{2+} (corresponding to pressures ranging from 0.1 – 1 bar) and reaches a maximum at a value of $\sim 10^{-8}$ m^2/s before decreasing gradually with increasing pressure (Figure 3).

Both the NMR data and simulations reveal that the magnitude of D_s is inversely related to the binding energy at the coordinatively unsaturated metal sites ($U_{binding}$: Ni > Mg > Zn) — that is, self-diffusion is fastest in Zn_2(dobdc) and slowest in Ni_2(dobdc). We also observe that the methane heat of adsorption increases with increasing methane loading in the pores up until a loading of ~ 0.8 CH_4/M^{2+} (Figure S3). It might readily be interpreted from this result that the diffusion coefficient should also decrease with increasing methane uptake in this regime. However, as can be seen from Figure 3, the D_s coefficients initially increase in all three metal frameworks at very low loadings (< 0.16 CH_4/M^{2+}). This increase can be explained by considering the free energy barriers between two metal sites in a given "slice" along the *ab*-plane. Because methane diffuses down the pore by hopping along nearby metal sites, either down the *z*-axis or in a "ring-like" fashion along a given *ab*-slice (Figure 7), a lower free energy barrier between two primary adsorption sites located along the *z*-axis will lead to a greater D_s coefficient. We have calculated this free energy barrier from the MD trajectories and indeed found that having more methane molecules in the pores lowers the

free energy barrier for methane hopping between open metal sites along the z-axis at low loadings (Figure 4).

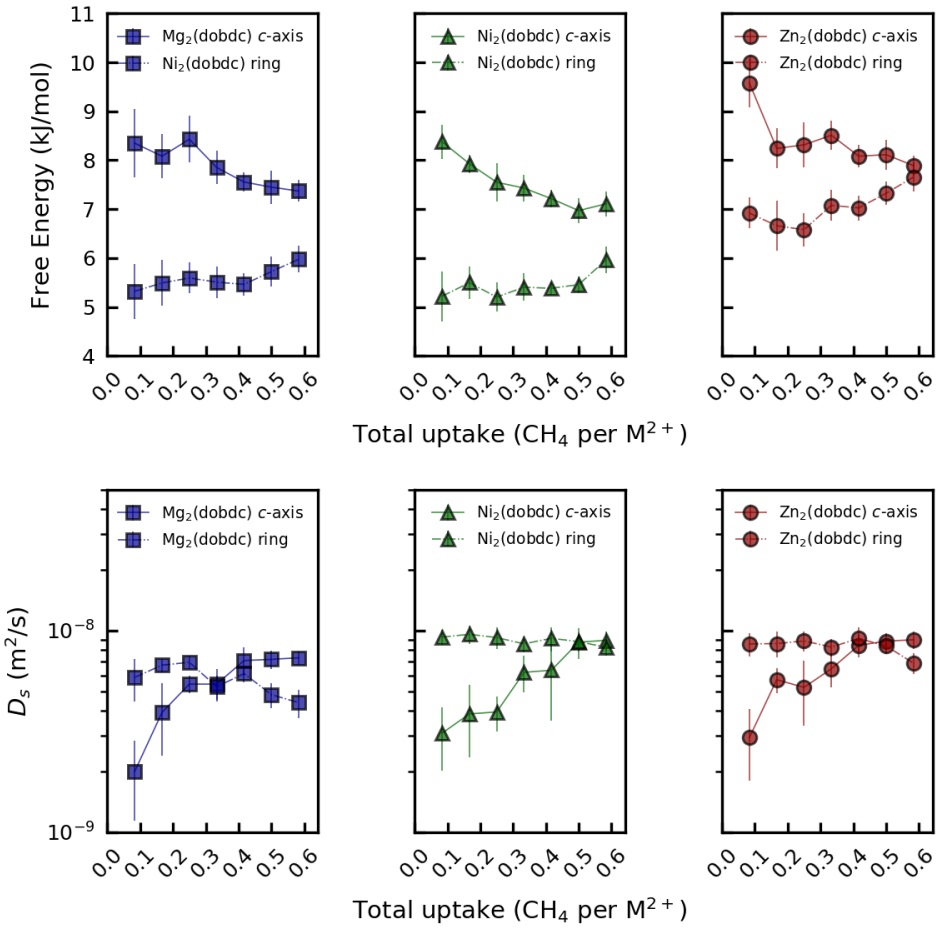

Figure 4: Free energy barriers (top) and diffusion coefficients D_s (bottom) between open metal sites in M_2(dobdc) (M = Mg, Ni, and Zn). The label "c-axis" indicates the free energy barriers and D_s for hopping between two open metal sites along a given c-axis, whereas the label "ring" indicates the free energy barriers and D_s for hopping between metal sites on a given ab-slice of the framework. Note that D_s for the ring transitions does not indicate true diffusion. All reported values are averages, and each error bar is the standard deviation of six free energy barriers and D_s, respectively, calculated from a single MD simulation.

To illustrate how, at very low loadings, the presence of a second CH_4 molecule lowers the free energy barrier for hopping from one metal site to another, we have calculated the free energy profiles from simulations with and without a rigid CH_4 already bound at the open metal site (Figure 5). The values of the free energy at the corresponding transition states

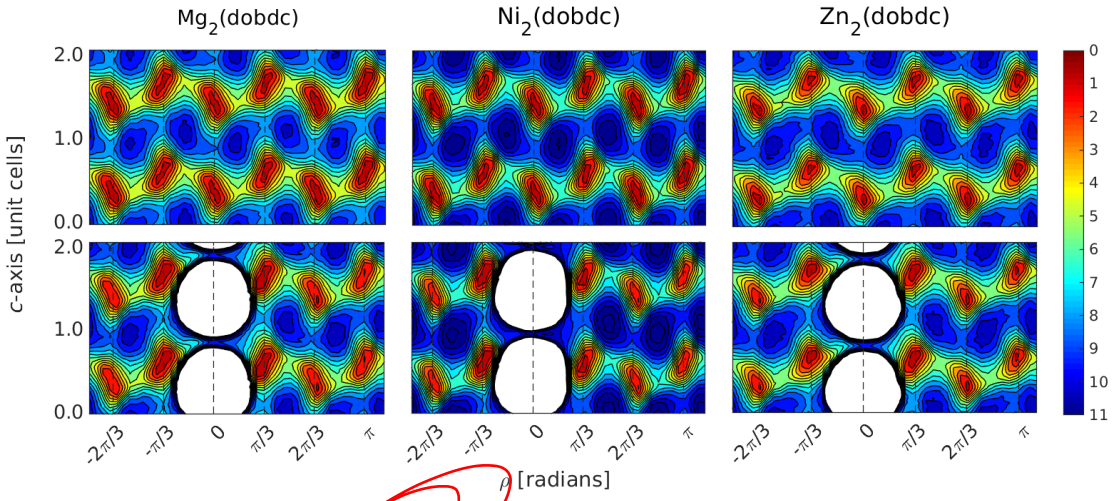

Figure 5: Free energy distributions in cylindrical coordinates integrated and normalized over radius values derived from MC simulations without (top) and with (bottom) a rigid CH_4 located at the minimum energy site at 0 radians.

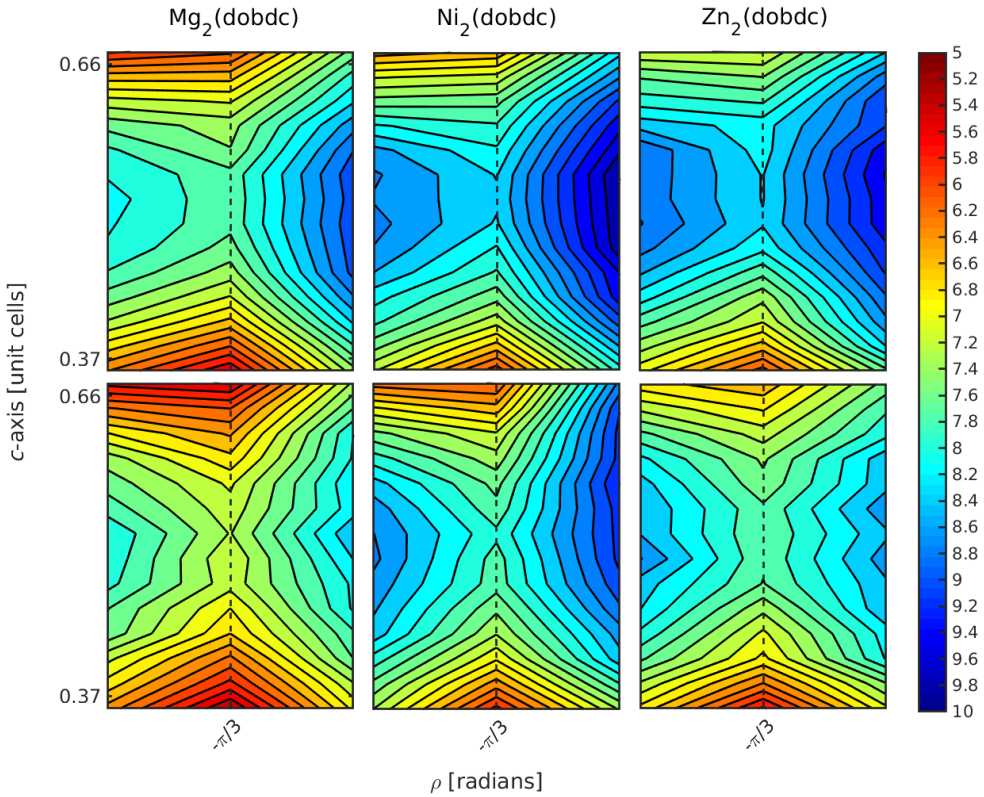

Figure 6: Free energy distributions in cylindrical coordinates integrated and normalized over radius values derived from MC simulations without (top) and with (bottom) a rigid CH_4 located at the minimum energy site at 0 radians. Zoomed in on transitions in the direction of the c-axis

Table 1: Energy barriers for transitions between primary binding sites along the c-axis. Values are given in kJ/mol and are averaged over equivalent transitions. For the empty framework structure (FW) the average is over 6 transitions and for the CH_4 enriched structure (FW + CH_4) averages are over 2, 2 and 1 transitions at angles $|\rho| = \pi/3,\ 2\pi/3$ and π radians, respectively, relative the added rigid CH_4 particle in the framework.

	Mg	**Ni**	**Zn**
FW	7.6	8.3	8.1
FW + 1 CH_4, $\|\rho\| = \pi/3$	7.4	8.1	7.7
FW + 1 CH_4, $\|\rho\| = 2\pi/3$	7.6	8.3	8.0
FW + 1 CH_4, $\|\rho\| = \pi$	7.7	8.4	8.1

from these simulations are given in Table 1. Indeed, what we observe is that for transitions at angles $|\rho| = \pi/3$, the free energy barrier is lower in all three frameworks. Figure 6 zooms in on the free energy barriers for transitions along the c-axis at angles $|\rho| = \pi/3$, illustrating how the two free energy wells meet first in the Ni framework, followed by the Mg framework, and finally the Zn framework; it also illustrates further how the free energy is overall lower when there is already a CH_4 bound at the open metal site.

These results are in contrast to our initial hypothesis, where the sharp increase in D_s at low loadings was originally thought to be due to more CH_4 in the pores effectively blocking the metal sites, thus shielding other CH_4 molecules from these strong binding sites and allowing them to diffuse past without binding. However, probability density maps show that the methane spends most of its time above the metal sites in simulations at both of these densities (Figure 7), and in fact the results at both densities look very similar, eliminating this as a possible mechanism and leading us to investigate the aforementioned free energy calculations.

Although the diffusivities calculated from simulations differ from experimentally measured values by an order of magnitude, the intracrystalline D_s values display similar trends with respect to the changes in their magnitudes at loadings greater than 0.16 CH_4/M^{2+}. It is important to note that the maximum in D_s occurs at a loading of $\sim$ 0.16 CH_4/M^{2+} for all frameworks considered herein. The initial increase in D_s can thus be explained by the growing presence of CH_4 molecules in the pores where there are initially not enough CH_4

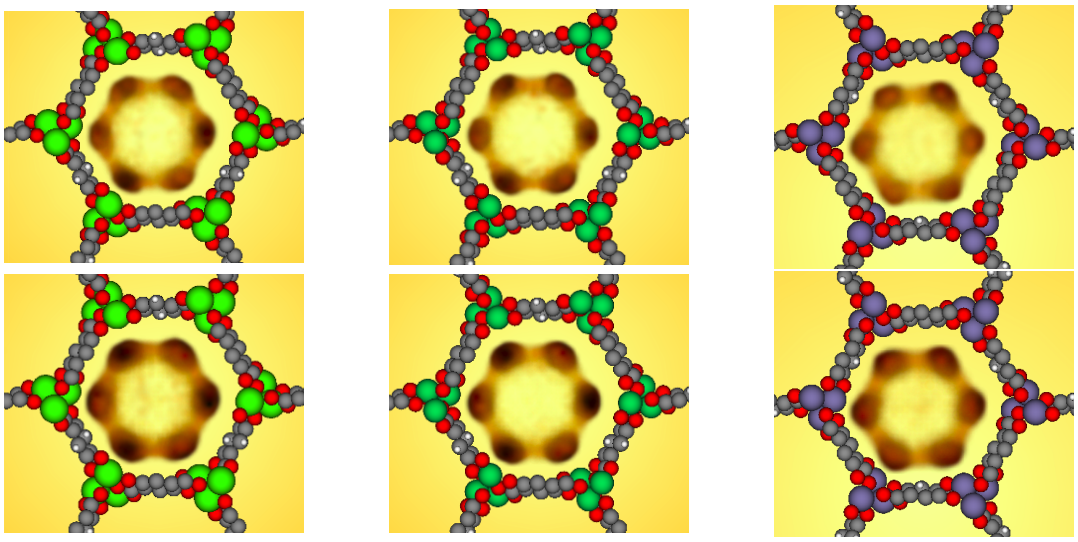

Figure 7: Probability densities of methane in M_2(dobdc) (M = Mg, Ni, and Zn) as derived from MD simulations with 4 CH_4/M^{2+} (top) and 14 CH_4/M^{2+} (bottom). Dark orange clouds represent the position of methane centers-of-mass throughout the simulation binned into a 0.2 $\AA$ grid. Light green, dark green, purple, gray, red, and white spheres represent Mg, Ni, Zn, C, O, and H atoms, respectively.

molecules to stabilize not only the adsorption sites, but also the transition states for hopping between one metal site to another. After the maximum in D_s is reached, an increase in the frequency of CH_4–CH_4 collisions in the pores leads to an increase in the drag force on CH_4 molecules, thus lowering their mean-squared displacements.

As discussed in the *Methods* section, at the lowest CH_4 loadings considered in this work ($\sim$ 0.027 CH_4/M^{2+}), simulations would consist of boxes containing only one or two CH_4 molecules if carried out in the same way as those simulations at the higher loadings, which would be problematic from the simulation point of view. As such, various fixed-density simulations were carried out that would allow us to extrapolate to an infinitely-large simulation box. In fact, as a result of these constant-density simulations at low uptakes, we find that as the number of molecules in the simulation box increases at a fixed density, the self-diffusion coefficients slowly increase until converging, as illustrated in Figure 8.

The magnitude of D_s converge faster for simulations involving $2N$ CH_4 atoms per pore compared to N CH_4 atoms per pore, which is expected. As shown by the y-intercepts of

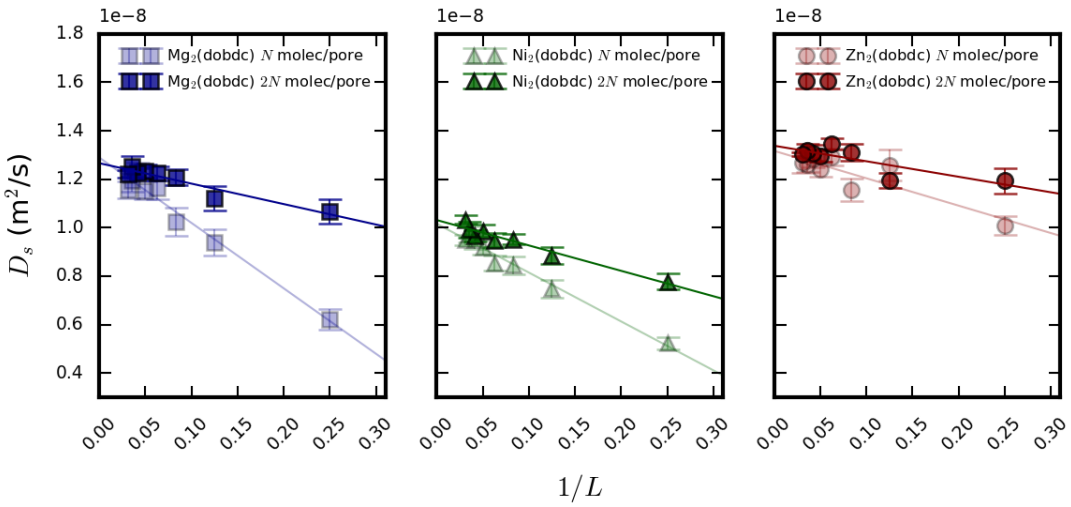

Figure 8: Simulated values of the methane self-diffusion coefficient, D_s, in M_2(dobdc) (M = Mg, Ni, and Zn) calculated at low, constant densities as a function of $1/L$, where L is the number of periodic replicas along the framework c-axis. The densities of CH_4 in each framework correspond to a loading of 0.027 CH_4/M^{2+} for each N molec/Å^3 dataset, and to a loading of 0.055 CH_4/M^{2+} for each $2N$ molec/Å^3 dataset (details in Table 2). The colored lines indicate linear fits to the data.

the linear fits in Figure 8, which extrapolate the diffusion coefficient to an infinitely-long simulation box, the value of D_s is greatest in the Zn framework and smallest in the Ni framework at low CH_4 densities D_s (1.266e-8, 1.032e-8, and 1.338e-8 m^2/s for Mg, Ni, and Zn, respectively). This trend is also in agreement with that found for D_s from simulations at larger densities (Figure 3), as the D_s is found to be inversely related to the CH_4 binding energy at the coordinatively unsaturated metal sites in each framework.

Table 2: Methane densities in molecules per Å^3 used in the low-density simulations. In these simulations, the number of CH_4 molecules and number of unit cell replicas was varied, but the densities remained the same. A density of N molecules per Å^3 corresponds to a value of 0.027 CH_4/M^{2+}, and a density of $2N$ molec per Å^3 corresponds to a value of 0.055 CH_4/M^{2+}.

	Mg	**Ni**	**Zn**
N molec per Å^3	2.988×10^{-4}	3.048×10^{-4}	3.039×10^{-4}
$2N$ molec per Å^3	5.976×10^{-4}	6.096×10^{-4}	6.078×10^{-4}

Conclusion

We have used a combination of NMR and computational studies to elucidate a relationship between the strength of methane binding at the coordinatively unsaturated metal sites in the frameworks M_2(dobdc) (M = Mg, Ni, and Zn) and the dynamics of adsorbed CH_4. In this work, the MD simulations were particularly key to fully understanding the diffusion of CH_4 at very low densities that are not accessible experimentally.

From NMR experiments, we observed for the first time a non-linear regime for the spin-lattice relaxation rate, R_1, of adsorbed methane gas, which we attributed to a weighted contribution of the spin rotation mechanism and the intermolecular dipole-dipole interactions to the characteristic rotational correlation time of the system. We demonstrated for the first time in an isoreticular MOF series that the strength of interaction between methane and the coordinatively unsaturated metal sites increases rotational correlation times at low densities due to translation displacement mediated by adsorption interactions. These findings support the continued use of loading dependent relaxometry studies to discern differences in surface interactions between adsorbate and adsorbent.

Two D_s coefficients were observed experimentally for all frameworks and loadings. Although differing by an order of magnitude, the slow D_s coefficient arising from intracrystalline diffusion is in reasonable agreement with the D_s coefficients calculated from simulations when considering the relative differences in the magnitudes of both sets of D_s coefficients for each M_2(dobdc) analogue.

Simulation data at higher loadings suggested that favorable CH_4–CH_4 interactions at higher pressures and a greater number of collisions cause the D_s values to steadily decrease. Simulation data at low loadings revealed that the self-diffusion coefficient slowly increases until it reaches a maximum in all three structures; we attribute this increase to a stabilization of the free energy barrier for hopping between two open metal sites due to the presence of additional methane molecules. This result is interesting because the heat of adsorption of methane in M_2(dobdc) also becomes more favorable as more methane adsorbs in the frame-

work, but this does not lead to methane becoming more localized due to the simultaneous stabilization of the free energy barrier for hopping between open metal sites along the z-direction. This increase in D_s is only noticable until a loading corresponding to a single CH_4 molecule per six metal sites, where the D_s values are maximized.

At very low CH_4 loadings (~ 0.027 CH_4/M^{2+}), simulations of CH_4 in M_2(dobdc) were carried out in increasingly larger and larger simulation boxes (keeping the CH_4 density in the pores fixed) to show that as we increase the number of molecules in the simulation box while keeping the densities fixed, the self-diffusion coefficients slowly increase until converging at a constant value. We attributed this behavior to an increase in the number of intermolecular collisions at these very dilute densities when there are simply more adsorbents in the simulation box.

Finally, the magnitudes of the intracrystalline CH_4 D_s coefficients are overall smallest in Ni_2(dobdc) and largest in Zn_2(dobdc). This is because the coordinatively unsaturated metal sites interact more strongly with adsorbed CH_4 in the Ni_2(dobdc) framework and more weakly in the Zn_2(dobdc) framework; the stronger a CH_4 molecule adsorbs to the framework, the less distance it can travel over a fixed amount of time. Simulations and experiments are in agreement with the trend in the D_s coefficients predicted at the higher methane loadings studied.

We note that none of the computational studies presented here would have been possible without parameterization of the DFT-derived force field reported previously,[16] illustrating the value of having inexpensive yet accurate models of adsorption in promising nanoporous materials for the comprehensive study of adsorbate thermodynamics. From an experimental standpoint, NMR facilitates a valuable systematic study of the effect of host-guest energetics on adsorbate diffusion in metal–organic frameworks. The comprehensive and improved understanding of adsorbate behavior at the atomic scale using these complementary techniques reinforces the concept of combined experimental-computational studies can be very valuable in guiding the improved design of materials for gas separation applications, especially when

seeking to understand adsorption and diffusion behavior at the atomic scale.

Acknowledgement

This work was supported as part of the Center for Gas Separations Relevant to Clean Energy Technologies, as an Energy Frontier Research Center funded by the U.S. Department of Energy, Office of Science, Basic Energy Sciences under Award DE-SC0001015. V.J.W. and R.M. acknowledge support by the National Science Foundation under both grant numbers DGE 1752814 and DGE 1106400. This research also used resources of the National Energy Research Scientific Computing Center, a DOE Office of Science User Facility supported by the Office of Science of the U.S. Department of Energy under Contract No. DE-AC02-05CH11231. We also thank ACalNet, the Aachen-California Network of Academic Exchange (DAAD Germany), for supporting the research visit of V.J.W. to RWTH Aachen University, and Dr. Katie R. Meihaus for editorial assistance.

References

(1) Tanabe, K. K.; Wang, Z.; Cohen, S. M. Systematic functionalization of a metal- organic framework via a postsynthetic modification approach. *J. Am. Chem. Soc.* **2008**, *130*, 8508–8517.

(2) Wang, Z.; Cohen, S. M. Postsynthetic modification of metal–organic frameworks. *Chem. Soc. Rev.* **2009**, *38*, 1315–1329.

(3) Morris, W.; Doonan, C. J.; Yaghi, O. M. Postsynthetic modification of a metal–organic framework for stabilization of a hemiaminal and ammonia uptake. *Inorg. Chem.* **2011**, *50*, 6853–6855.

(4) Wang, C.; Liu, D.; Lin, W. Metal-organic Frameworks as a Tunable Platform for Designing Functional Molecular Materials. *J. Am. Chem. Soc.* **2013**, 130814191409007.

(5) Marshall, R. J.; Forgan, R. S. Postsynthetic Modification of Zirconium Metal-Organic Frameworks. *Eur. J. Inorg. Chem.* **2016**, *2016*, 4310–4331.

(6) Rungtaweevoranit, B.; Diercks, C. S.; Kalmutzki, M. J.; Yaghi, O. M. Spiers Memorial Lecture: Progress and prospects of reticular chemistry. *Faraday Discuss.* **2017**, *201*, 9–45.

(7) Zhou, H.-C.; Long, J. R.; Yaghi, O. M. Introduction to Metal–Organic Frameworks. *Chem. Rev.* **2012**, *112*, 673–674.

(8) Furukawa, H.; Cordova, K. E.; O'Keeffe, M.; Yaghi, O. M. The chemistry and applications of metal-organic frameworks. *Science* **2013**, *341*, 1230444.

(9) Peng, Y.; Krungleviciute, V.; Eryazici, I.; Hupp, J. T.; Farha, O. K.; Yildirim, T. Methane storage in metal-organic frameworks: current records, surprise findings, and challenges. *J. Am. Chem. Soc.* **2013**, *135*, 11887–94.

(10) Mason, J. A.; Veenstra, M.; Long, J. R. Evaluating metal–organic frameworks for natural gas storage. *Chem. Sci.* **2014**, *5*, 32–51.

(11) Kuppler, R. J.; Timmons, D. J.; Fang, Q.-R.; Li, J.-R.; Makal, T. a.; Young, M. D.; Yuan, D.; Zhao, D.; Zhuang, W.; Zhou, H.-C. Potential applications of metal-organic frameworks. *Coord. Chem. Rev.* **2009**, *253*, 3042–3066.

(12) Sumida, K.; Rogow, D. L.; Mason, J. A.; McDonald, T. M.; Bloch, E. D.; Herm, Z. R.; Bae, T.-H.; Long, J. R. Carbon dioxide capture in metal–organic frameworks. *Chem. Rev.* **2011**, *112*, 724–781.

(13) Queen, W. L. et al. Comprehensive study of carbon dioxide adsorption in the metal–organic frameworks M2 (dobdc)(M= Mg, Mn, Fe, Co, Ni, Cu, Zn). *Chem. Sci.* **2014**, *5*, 4569–4581.

(14) Simon, C. M.; Kim, J.; Gomez-Gualdron, D. A.; Camp, J. S.; Chung, Y. G.; Martin, R. L.; Mercado, R.; Deem, M. W.; Gunter, D.; Haranczyk, M.; Sholl, D. S.; Snurr, R. Q.; Smit, B. The materials genome in action: identifying the performance limits for methane storage. *Energy Environ. Sci.* **2015**, *8*, 1190–1199.

(15) Schoedel, A.; Ji, Z.; Yaghi, O. M. The role of metal–organic frameworks in a carbon-neutral energy cycle. *Nat. Energy* **2016**, *1*, 16034.

(16) Mercado, R.; Vlaisavljevich, B.; Lin, L.-C.; Lee, K.; Lee, Y.; Mason, J. A.; Xiao, D. J.; Gonzalez, M. I.; Kapelewski, M. T.; Neaton, J. B.; Smit, B. Force field development from periodic density functional theory calculations for gas separation applications using metal–organic frameworks. *J. Phys. Chem. C* **2016**, *120*, 12590–12604.

(17) Wu, H.; Zhou, W.; Yildirim, T. High-capacity methane storage in metal-organic frameworks M2(dhtp): The important role of open metal sites. *J. Am. Chem. Soc.* **2009**, *131*, 4995–5000.

(18) Lee, K.; Howe, J. D.; Lin, L.-C.; Smit, B.; Neaton, J. B. Small-molecule adsorption in open-site metal–organic frameworks: a systematic density functional theory study for rational design. *Chem. Mater.* **2015**, *27*, 668–678.

(19) Sutrisno, A.; Huang, Y. Solid-state NMR: a powerful tool for characterization of metal-organic frameworks. *Solid State Nucl. Magn. Reson.* **2013**, *49-50*, 1–11.

(20) Chen, D. L.; Shang, H.; Zhu, W.; Krishna, R. Reprint of: Transient breakthroughs of CO_2/CH_4 and C_3H_6/C_3H_8 mixtures in fixed beds packed with Ni-MOF-74. *Chem. Eng. Sci.* **2015**, *124*, 109–117.

(21) Kaerger, J.; Caro, J.; Cool, P.; Coppens, M.-O.; Jones, D.; Kapteijn, F.; Rodríguez-Reinoso, F.; Stoecker, M.; Theodorou, D.; Vansant, E. F.; Others, Benefit of microscopic diffusion measurement for the characterization of nanoporous materials. *Chem. Eng. and Technol.* **2009**, *32*, 1494–1511.

(22) Pusch, A.-K.; Splith, T.; Moschkowitz, L.; Karmakar, S.; Biniwale, R.; Sant, M.; Suffritti, G. B.; Demontis, P.; Cravillon, J.; Pantatosaki, E.; Stallmach, F. NMR studies of carbon dioxide and methane self-diffusion in ZIF-8 at elevated gas pressures. *Adsorption* **2012**, *18*, 359–366.

(23) Stallmach, F.; Gröger, S.; Künzel, V.; Kärger, J.; Yaghi, O. M.; Hesse, M.; Müller, U. NMR studies on the diffusion of hydrocarbons on the metal-organic framework material MOF-5. *Angew. Chem. Int. Ed. Engl.* **2006**, *45*, 2123–6.

(24) Kong, X.; Scott, E.; Ding, W.; Mason, J. A.; Long, J. R.; Reimer, J. A. CO_2 dynamics in a metal-organic framework with open metal sites. *J. Am. Chem. Soc.* **2012**, *134*, 14341–4.

(25) Lin, L.-C.; Kim, J.; Kong, X.; Scott, E.; McDonald, T. M.; Long, J. R.; Reimer, J. A.; Smit, B. Understanding CO2 dynamics in metal–organic frameworks with open metal sites. *Angewandte Chemie* **2013**, *125*, 4506–4509.

(26) Stallmach, F.; Pusch, A.-K. K.; Splith, T.; Horch, C.; Merker, S. NMR relaxation and diffusion studies of methane and carbon dioxide in nanoporous ZIF-8 and ZSM-58. *Microporous Mesoporous Mater.* **2015**, *205*, 36–39.

(27) Forse, A. C.; Gonzalez, M. I.; Siegelman, R. L.; Witherspoon, V. J.; Jawahery, S.; Mercado, R.; Milner, P. J.; Martell, J. D.; Smit, B.; Blumich, B.; Long, J. R.; Reimer, J. A. Unexpected Diffusion Anisotropy of Carbon Dioxide in the Metal–Organic Framework Zn2 (dobpdc). *J. Am. Chem. Soc.* **2018**, *140*, 1663–1673.

(28) Chmelik, C. Characteristic Features of Molecular Transport in MOF ZIF-8 as revealed by IR Microimaging. *Microporous Mesoporous Mater.* **2015**,

(29) Krishna, R.; van Baten, J. M. Influence of adsorption thermodynamics on guest diffusivities in nanoporous crystalline materials. *Phys. Chem. Chem. Phys.* **2013**, *15*, 7994–8016.

(30) Bachman, J. E.; Kapelewski, M. T.; Redd, D. A.; Gonzalez, M. I.; Long, J. R. M_2(m-dobdc)(M = Mn, Fe, Co, Ni) Metal Organic Frameworks as a Highly Selective, High-Capacity Adsorbents for Olefin/Parraffin Separations. *J. Am. Chem. Soc.* **2017**, *139*, 15363–15370.

(31) Cotts, R. M.; Hoch, M. J. R.; Sun, T.; Markert, J. T. I. Pulsed Field Gradient Stimulated Echo Methods for Improved NMR Diffusion Measurements in Heterogeneous Systems. *J. Magn. Reson.* **1989**, *266*, 252–266.

(32) Casanova, F.; Perlo, J.; Blümich, B. *Single-Sided NMR*; Springer, 2011; pp 1–10.

(33) Callaghan, P. NMR imaging, NMR diffraction and applications of pulsed gradient spin echoes in porous media. *Magn. Reson. Imaging* **1996**, *14*, 701–709.

(34) Plimpton, S. Fast Parallel Algorithms for Short Range Molecular Dynamics. *J. Comput. Phys.* **1995**, *117*, 1–42.

(35) Sandia National Labs, LAMMPS. `http://lammps.sandia.gov`, using July 30, 2016 release throughout this work.

(36) Martin, M. G.; Siepmann, J. I. Transferable potentials for phase equilibria. 1. United-atom description of n-alkanes. *J. Phys. Chem. B* **1998**, *102*, 2569–2577.

(37) Dubbeldam, D.; Ford, D.; Ellis, D.; Snurr, R.; Dubbeldam, D.; Ford, D.; Ellis, D.; Snurr, R.; Perspective, A. N. A New perspective on the Order-n Algorithm for Computing Correlation Functions. *Mol. Simul.* **2009**, *35*, 1084–1097.

(38) Frenkel, D.; Smit, B. *Understanding molecular simulation: from algorithms to applications*; Elsevier, 2001; Vol. 1.

(39) Simon, C. PEGrid. 2017; `https://github.com/CorySimon/PEGrid`.

(40) Childs, H. et al. *High Performance Visualization–Enabling Extreme-Scale Scientific Insight*; 2012; pp 357–372.

(41) Bennett, C. H. Molecular dynamics and transition state theory: the simulation of infrequent events. *Algorithms Chem. Comp.* **1977**, *46*, 63–97.

(42) Chandler, D. Statistical mechanics of isomerization dynamics in liquids and the transition state approximation. *J. Chem. Phys.* **1978**, *68*, 2959–2970.

(43) Jackowski, K.; Jaszunski, M. In *Gas Phase NMR*; Jackowski, K., Jaszunski, M., Eds.; Royal Society of Chemistry: Cambridge, UK, 2016.

(44) Gerritsma, C.; OOsting, P.; Trappeniers, N. J. Proton-spin-lattice and self-diffusion in Methanes. *Physica* **1971**, *51*, 381–394.

(45) Kowalewski, J. *Nuclear Spin Relaxation in Diamagnetic Fluids. Part 1. General Aspects and Inorganic Applications*; 1990; Vol. 22; pp 307–414.

(46) McClung, R. Spin–rotation relaxation theory. *eMagRes* **2007**,

(47) Bloom, M.; Lipsicas, M.; Muller, B. PROTON SPIN-LATTICE RELAXATION IN POLYATOMIC GASESL. *Can. J. Phys.* **1961**, *39*.

(48) Stapf, S.; Kimmich, R.; Seitter, R.-O. Proton and deuteron field-cycling NMR relaxometry of liquids in porous glasses: evidence for Lévy-walk statistics. *Phys. Rev. Lett.* **1995**, *75*, 2855.

(49) Xiang, S.; He, Y.; Zhang, Z.; Wu, H.; Zhou, W.; Krishna, R.; Chen, B. Microporous metal-organic framework with potential for carbon dioxide capture at ambient conditions. *Nat. Commun.* **2012**, *3*, 954.